Soft Matter

PAPER

View Article Online
View Journal | View Issue

Cite this: *Soft Matter*, 2023, **19**, 8434

Droplet detachment force and its relation to Young–Dupre adhesion†

Dan Daniel *[a] and Xue Qi Koh[b]

Received 3rd September 2023,
Accepted 19th October 2023

DOI: 10.1039/d3sm01178j

rsc.li/soft-matter-journal

Droplets adhere to surfaces due to their surface tension γ and understanding the vertical force F_d required to detach the droplet is key to many technologies (*e.g.*, inkjet printing, optimal paint formulations). Here, we predicted F_d on different surfaces by numerically solving the Young–Laplace equation. Our numerical results are consistent with previously reported results for a wide range of experimental conditions: droplets subjected to surface *vs.* body forces with $|F_d|$ ranging from nano- to milli-newtons, droplet radii R ranging from tens of microns to several millimetres, and for various surfaces (micro-/nano-structured superhydrophobic *vs.* lubricated surfaces). Finally, we derive an analytic solution for F_d on highly hydrophobic surfaces and further show that for receding contact angle $\theta_r > 140°$, the normalized $F_d/\pi R$ is equivalent to the Young–Dupre work of adhesion $\gamma(1 + \cos\theta_r)$.

We encounter the effects of droplet adhesion every day: dew of droplets can be seen clinging to blades of grass in early morning, and droplets stuck to camera lenses affect image clarity on rainy/misty days.[1,2] Despite the prevalence of the phenomenon and clear importance in various technologies (from inkjet printing[3] to agricultural technologies[4,5]), there is still no consensus on how to link the vertical force F_d required to detach a droplet from a surface to its wetting properties.[6–9] For example, Tadmor *et al.* (2017) proposed that $F_d/2\pi r$ (where r is the contact radius) is equivalent to the Young–Dupre work of adhesion $\gamma(1 + \cos\theta_r)$ where γ is the surface tension and θ_r is the receding contact angle,[10] but others disagreed.[11–13]

Extensive experimental data for droplet detachment exist in the literature,[10,13–17] but their interpretation is complicated by the fact that various groups use very different methods to measure F_d (Fig. 1) with very different droplet volumes (V = 5 pL–10 μL) and detachment speeds ($U = 10^{-6}$–10^{-3} m s^{-1}). As a result, different groups reported force magnitudes that vary considerably from 38 nN (as measured using atomic force microscopy or AFM) to 1.8 μN (force microbalance),[7] and 0.36 mN (centrifugal adhesion balance or CAB).[10] We will show later that the various datasets are in broad agreement with one another once F_d is normalized by the droplet radius R. The various approaches described in the literature can be broadly categorized into surface *vs.* body force methods—an important distinction that is often ignored. Methods such as AFM and microbalance force sensor (Fig. 1A and B) apply a pulling force only at the top surface of the droplet, *i.e.*, surface force. In contrast, in CAB (and other methods[18]), the centrifugal pulling force is applied to the entire droplet, *i.e.*, body force.

In this paper, we show that the quasi-static approximation applies during the retraction process for slow detachment speeds, and that F_d can be predicted by numerically solving the Young–Laplace equation.[19] Our numerical results are consistent with the experimental data collected independently by various research groups. We derive an analytic solution for F_d and further show that for a droplet of radius R the normalized $F_d/\pi R$ (as opposed to $F_d/2\pi r$) is equivalent to the Young–Dupre work of adhesion $\gamma(1 + \cos\theta_r)$ for highly hydrophobic surfaces

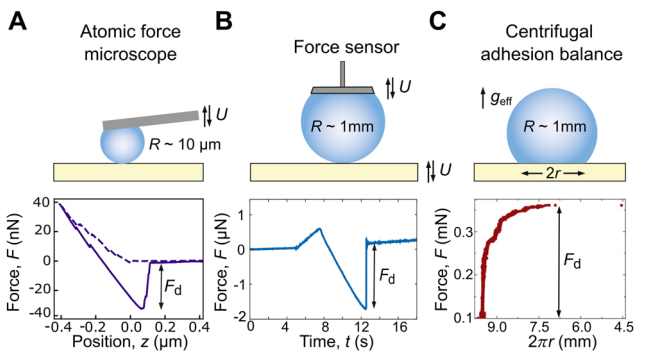

Fig. 1 Different methods to measure droplet detachment force F_d using (A) atomic force microscope (volume V = 65 pL, U = 2 μm s^{-1}, superhydrophobic surface), (B) microbalance force sensor (V = 5 μL, U = 5 μm s^{-1}, superhydrophobic surface), and (C) centrifugal adhesion balance (V = 10 μL, hydrophobic). A is original unpublished data, while B and C are taken from Daniel *et al.* (2023)[7] and Tadmor *et al.* (2017),[10] respectively.

[a] *Division of Physical Sciences and Engineering, King Abdullah University of Science and Technology (KAUST), Thuwal 23955-6900, Saudi Arabia. E-mail: danield@kaust.edu.sa*
[b] *Institute of Materials Research and Engineering, Agency for Science, Technology and Research (A*STAR), 138634, Singapore*

† Electronic supplementary information (ESI) available. See DOI: https://doi.org/10.1039/d3sm01178j

with $\theta_r > 140^\circ$. In contrast, for less hydrophobic surfaces with $\theta_r < 140^\circ$ there is no simple way to relate F_d to the Young–Dupre work of adhesion.

Our analysis is general and applies for a wide range of experimental conditions (including those in Fig. 1) and different surfaces (flat, micro-/nano-structured superhydrophobic,[20] and lubricated surfaces[21,22]).

1 Methods

1.1 Surface preparation

To make the superhydrophobic surface in Fig. 5A, we started with a 3 mm thick Sylgard 184 polydimethylsiloxane (PDMS) slab. We used a 10 : 1 monomer to linker ratio which was cured by heating the mixture at 70 °C for 3 hours. We then spraycoated the cured PDMS slab with a layer of hydrophobic nanoparticles (Glaco Mirror Coat Zero, Soft 99 Co.) before placing it vertically to dry for one hour before use. Note that the wetting properties of the resulting surface is dominated by the structured nanoparticles. We chose to use a PDMS slab as the base so that we can easily puncture the surface with a 34 Gauge needle (see Section 1.1.1). Scanning electron micrograph of the resulting nanostructures can be found in Fig. 1 of our previous publication.[23]

To make the lubricated surface in Fig. 5B, we coated a thin layer of fluorinated oil (GPL Krytox 101, ~3 μm thick, viscosity $\eta = 30$ mPa s^{-1}) onto the nanostructured PDMS slab.

1.1.1 Measuring detachment force. To measure the detachment force using AFM, please see our previous publications.[14,24] We also measure detachment force due to gravity by first puncturing the PDMS slab with a 34 Gauge needle (outer diameter of 0.16 mm), placing the surface upside down, and using a syringe pump to slowly increase the droplet volume until the droplet detaches (due to gravity).

1.1.2 Numerical simulations. To solve the axi-symmetric Young–Laplace equation, we use the shooting method implemented in the Python programming language. We have described the method at length in our previous publication.[14] Python codes used here are provided in github repositories.[25,26] Since we are solving for an axi-symmetric system, the contact angle value we use is necessarily a radially averaged value.

2 Results and discussions

Previously, different groups have suggested (implicitly[6] or explicitly[13,19]) that detachment results when the droplet is so stretched that it can no longer be described by the Young–Laplace equation. In contrast, Tadmor *et al.* (2017) suggest that the detachment force should be related to the Young–Dupre work of adhesion,[10] while others disagreed.[11–13] In this paper, we aim to reconcile these different views.

We start by numerically solving the axisymmetric Young–Laplace equation for a droplet subjected to either a surface force (Fig. 2) or a body force (Fig. 3). We can recast the Young–Laplace equation into its non-dimensional form by normalizing the various quantities with $V^{1/3}$ and surface tension γ (*e.g.*, $\tilde{u} = u/V^{1/3}$, $\Delta\tilde{P} = \Delta P V^{1/3}/\gamma$) to give

$$\begin{aligned} \frac{\tilde{u}''}{(1+\tilde{u}'^2)^{3/2}} - \frac{1}{\tilde{u}\sqrt{1+\tilde{u}'^2}} &= -\Delta\tilde{P} \quad \text{for } \tilde{z} \in (0, \tilde{h}) \\ \tilde{u}(\tilde{h}) &= \tilde{r} \\ \tilde{u}'(\tilde{h}) &= -\cot\theta_r \\ \int_0^{\tilde{h}} \pi\tilde{u}^2 \mathrm{d}\tilde{z} &= 1 \end{aligned} \tag{1}$$

where r is the droplet's contact radius and we assume that the droplet retracts with a constant receding contact angle θ_r.

For the surface force method, we can approximate the droplet geometry as being held by a circular disc with radius a at the top and further impose the boundary condition $\tilde{u}(0) = \tilde{a}$ (Fig. 2A) and assume that the Laplace pressure $\Delta\tilde{P} = \Delta\tilde{P}_0$ is constant (*i.e.*, we neglect the effects of gravity since the droplets are typically smaller than the capillary length). We performed numerical simulations for different $\theta_r = 40$–160° and fixed $\tilde{a} = 0.45$ (which approximates well the geometries used in various papers[14,15] including in Fig. 1A and B) and plotted the force acting on the droplet

$$\tilde{F} = -2\pi\tilde{r}\sin\theta + \pi\tilde{r}^2\Delta\tilde{P}_0 \tag{2}$$

(in its non-dimensional form) as we progressively stretched the droplet (Fig. 2B).

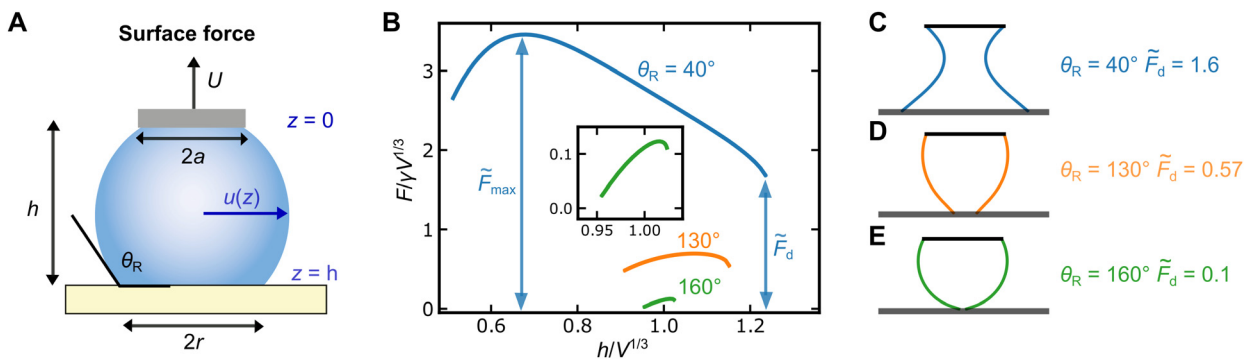

Fig. 2 (A) Schematic of a droplet attached to a disc of radius a and retracting from the surface. (B) Numerical solutions to Young–Laplace equation showing the non-dimensional force $F/\gamma V^{1/3}$ as a function of increasing $h/V^{1/3}$ for different contact angles $\theta_r = 40$–160°. Inset shows the magnified plot for $\theta_r = 160^\circ$. (C)–(E) Droplet geometries at the point of detachment for different θ_r.

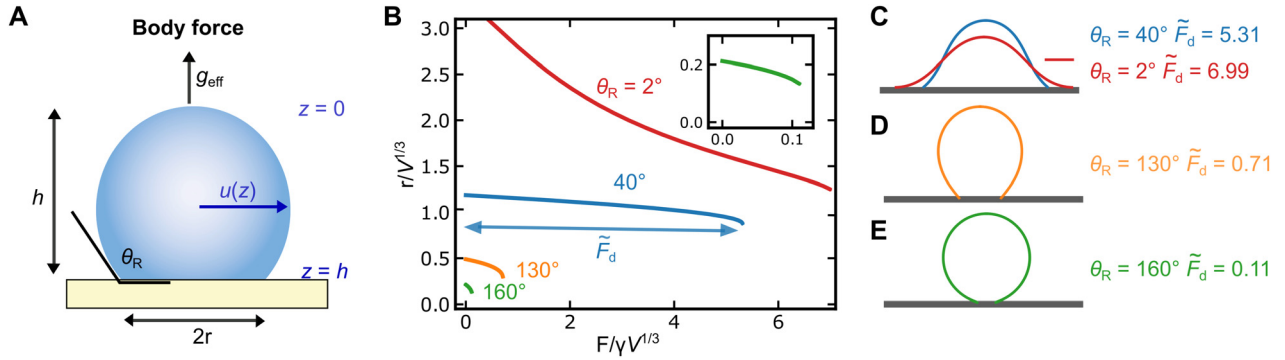

Fig. 3 (A) Schematic of a droplet of volume V and density ρ subjected to a body force $F = V\rho g_{eff}$ where g_{eff} is the effective acceleration. (B) Numerical solutions to Young–Laplace equation showing the non-dimensional contact radius $r/V^{1/3}$ as a function of increasing $F/\gamma V^{1/3}$ for different contact angles θ_r = 2–160°. Inset shows the magnified plot for θ_r = 160°. (C)–(E) Droplet geometries at the point of detachment for different θ_r. Scale bar in C is the non-dimensional capillary length $\sqrt{\tilde{F}_d} = 2.64$ for θ_r = 2°.

We terminate the simulations when we can no longer achieve numerical convergence; this is the point of droplet detachment and we can define the corresponding detachment force $\tilde{F}_d$ which strongly depends on θ_r, *i.e.*, the surface wetting properties. For hydrophilic surfaces, the detachment force is high ($\tilde{F}_d$ = 1.6 for θ_r = 40°) but can become negligible for superhydrophobic surfaces ($\tilde{F}_d$ = 0.1 for θ_r = 160°). For hydrophilic surfaces, the droplet is highly stretched at the point of detachment and resembles more of a capillary bridge (Fig. 2C). In contrast, the droplet retains its spherical cap shape till the point of detachment for highly hydrophobic surfaces (Fig. 2D and E).

Interestingly, the droplet experiences a maximum force $\tilde{F}_{max} > \tilde{F}_d$ before detaching. For hydrophilic surfaces, the two force quantities can be quite different, with $\tilde{F}_{max}/\tilde{F}_d$ = 2.2 for θ_r = 40° (Fig. 2B). In contrast, $\tilde{F}_{max}/\tilde{F}_d$ = 1.1 for θ_r = 160° (inset in Fig. 2B)

We now repeat the numerical simulations for a droplet subjected to an effective acceleration g_{eff} and an equivalent non-dimensional body force.

$$\tilde{F} = V^{2/3}\rho g_{eff}/\gamma. \quad (3)$$

The droplet geometry still obeys the Young–Laplace equation in eqn (1), except with different boundary conditions $\tilde{u}(0) = \tilde{u}'(0) = 0$ and with the Laplace pressure $\Delta\tilde{P} = \Delta\tilde{P}_0 - \tilde{F}\tilde{z}$ that varies with position $\tilde{z}$ (Fig. 3A).

We progressively stretch the droplets by increasing $\tilde{F}$ and noted the decrease in base radius $\tilde{r}$ for different θ_r = 2–160° (Fig. 3B). Note that $\tilde{F}$; is the input variable here, whereas it is the output variable in Fig. 2B. As is before, we terminate the simulations when there is no longer numerical convergence, and we can define the corresponding detachment force $\tilde{F}_d$ (but no $\tilde{F}_{max}$). For hydrophilic surfaces, the droplet resembles a spherical cap whose base is surrounded by a wetting skirt/meniscus of size $\sqrt{\tilde{F}_d}$ the non-dimensional capillary length (see scale bar in Fig. 3C). The wetting skirt is a low pressure region and provides the suction required to hold onto the droplet. In contrast, for highly hydrophobic surfaces, the droplet retains its spherical cap geometry (Fig. 3D and E).

We can check the validity of our simulation results by superimposing experimental data collected independently by five different research groups using different methodologies ranging from AFM,[14] microbalance force sensors,[15,16] and CAB.[10,13] When the normalized detachment force $F_d/\gamma V^{1/3}$ is plotted against $\varepsilon = 1 + \cos\theta_r$, all the experimental data are consistent with results from our numerical simulations for both surface and body forces (blue and red curves in Fig. 4A, respectively). We have also included results collected by us (open symbols in Fig. 4A), including previously unpublished results in Fig. 1A and 5.

Interestingly, the two master curves approach each other in the limit of $\theta_r > 140°$. In other words, F_d measurement is independent of the method chosen for highly hydrophobic surfaces with $\theta_r > 140°$. In contrast, for less hydrophobic surfaces with $\theta_r < 140°$, F_d measurement values depend strongly on the method chosen (surface *vs.* body forces), a point that is not well appreciated in the literature.

We have tabulated the simulation results in Table S1 (ESI†): we found that $\tilde{F}_d$ values for body and surface forces differ by 10% or less for $\theta_r > 140°$. For convenience, the numerical solutions of $\tilde{F}_d$ for surface and body force methods can be fitted globally with the polynomial functions

$$\frac{F_d}{\gamma V^{1/3}} = \begin{cases} 1.971\varepsilon - 0.961\varepsilon^2 + 0.190\varepsilon^3 & \text{surface} \\ 2.296\varepsilon - 0.791\varepsilon^2 + 0.696\varepsilon^3 & \text{body} \end{cases} \quad (4)$$

Note however that there are significant local deviation of the actual simulation results from the fitted polynomials in eqn (4). If we perform regression analysis only for $\theta > 140°$ (equivalently for $\varepsilon < 0.2$), we found that $\tilde{F}_d = 1.95\varepsilon$ for both body and surface forces. The slope of 1.95 has a simple physical interpretation which we will explore in the next section.

Relation of F_d to Young–Dupre work of adhesion

We can derive an analytic expression for F_d in terms of $\varepsilon = 1 + \cos\theta_r$ for $\varepsilon \ll 1$, *i.e.*, in the limit of $\theta_r \to 180°$. According to Young–Dupre, the energy required to detach the droplet is given by $\Delta E_\gamma = \pi r^2\gamma\varepsilon$, which assumes that the droplet retains its spherical cap geometry after detachment. This is a reasonable assumption for a frozen water droplet detaching from a cold surface,[28] but not for liquid droplets at room temperature.

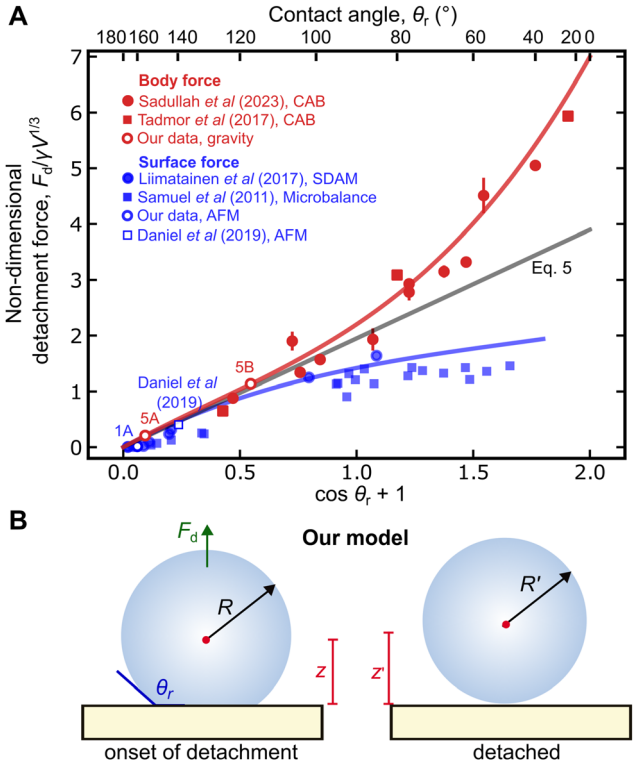

Fig. 4 (A) Plot of $F_d/\gamma V^{1/3}$ as a function of $(1 + \cos\theta_r)$. Unfilled data points are our experimental results corresponding to Fig. 1A and 5A, B and from our previous paper,[14] while filled data points are results from various groups.[10,13,15,16] (B) Droplet geometry during the detachment process for high θ_r. Raw dataset can be found in ref. 27.

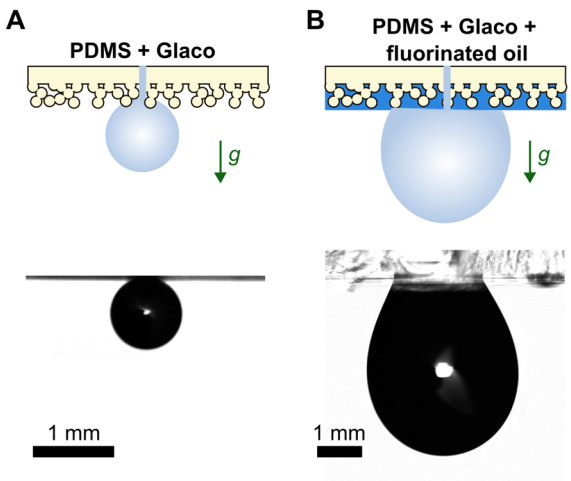

Fig. 5 Droplet detachment due to gravity. Water droplets at the point of detachment for (A) superhydrophobic and (B) lubricated surfaces. Raw dataset can be found in ref. 27.

In reality, the detached droplet adopts a spherical shape (Fig. 4B); using simple geometrical arguments and power series expression, we can show that $\Delta E_\gamma \approx \pi R^2\gamma\varepsilon^2$. At the same time, the droplet's centroid is raised by an amount $\delta z = z' - z \approx R\varepsilon$ (See full derivation in Fig. S1, ESI†).

Since the work done by the detachment force $F_d\delta z$ must be equal to ΔE_γ,

$$F_d = \pi R\gamma\varepsilon$$
$$\frac{F_d}{\gamma V^{1/3}} = \left(\frac{\pi}{2}\right)^{2/3} 3^{1/3}\varepsilon \approx 1.95\varepsilon \quad (5)$$

using the fact that $V = 4/3\pi R^3$ (Compare eqn (5) and (4)). The analytic expression in eqn (5) (gray curve in Fig. 4) agrees well with the experimental data and the two numerical solutions to Young–Laplace equation for $\varepsilon < 0.2$ or equivalently $\theta_r > 140°$. This is not surprising since for high θ_r, the droplet geometry is well approximated by a sphere (see Fig. 2D, E and 3D, E). See also Table S1 (ESI†).

For highly hydrophobic surface, the detachment force F_d when normalized by πR is therefore equivalent to $\gamma(1 + \cos\theta_r)$ the Young–Dupre work of adhesion (per unit area). This result is different from the scaling proposed by Tadmor *et al.* (2017) where the authors suggested that $F_d/2\pi r = \gamma(1 + \cos\theta_r)$.[10] For hydrophilic surfaces, there is no simple way to relate F_d to $\cos\theta_r$ since the droplet is highly deformed and its geometry depends on the choice of experimental method (compare Fig. 2C and 3C).

The results presented here are general and apply for a wide range of experimental conditions and surface types from superhydrophobic (Fig. 5A) to lubricated surfaces (Fig. 5B). In Fig. 5, we slowly increase the droplet volume until gravity (another example of body force) causes the droplet to detach from the surface. Eqn (5) correctly predicts the droplet weight $F_d = V\rho g$ at the point of detachment for both surfaces (see red open circles in Fig. 4). Note that there is a wrapping layer of the fluorinated oil for the droplet on lubricated surface (Fig. 5B),[29,30] and we used an effective surface tension $\gamma = 69$ mN m^{-1} when calkculating $F_d/\gamma V^{1/3}$. Strictly speaking, our approach is true only for lubricated surfaces with vanishingly small wetting ridge and when viscous dissipation due to the wetting ridge can be ignored. These two conditions were met in our experiment since we used a relatively thin lubricant layer of about 3 μm and relatively non-viscous lubricant of viscosity $\eta = 30$ mPa s.

Validity of quasi-static approximation

In our analysis so far, we have used the quasi-static approximation and assumed that the body force applied or the gap h is increased gradually such that F_d is dominated by surface wetting properties (in particular θ_r) and not by dynamic effects (*e.g.*, viscous dissipation). This is true for the cases described above and also explains why different groups reported that F_d is independent of U (at least for superhydrophobic surfaces).[14,15]

There are however cases where this assumption is not valid. For example, viscous dissipation can dominate for highly viscous or non-Newtonian liquids.[31] If the speed of detachment is faster than the speed at which the contact-line can recede, dynamical effects such as pinch-off instability can occur. Some underwater superoleophobic surface also exhibits $\theta_r = 180°$ (*i.e.*, no contact line pinning) and F_d is always dominated by viscous

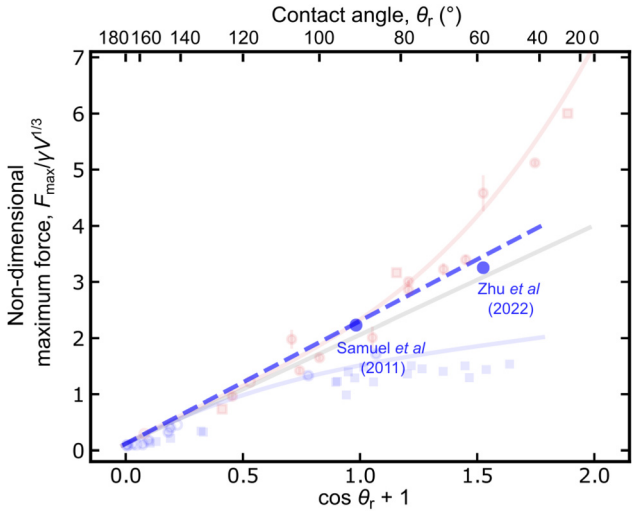

Fig. 6 Comparison between numerical results for $\tilde{F}_{max}$ (dashed blue line) and experimental results from Samuel *et al.* (2011)[16] and Zhu *et al.* (2022).[17] Results in Fig. 4 are also superimposed (in faint) for easy comparison.

dissipation even at low $U \sim$ μm s^{-1}. Previously, we showed that $F_d \propto U^{3/5}$ for an oil droplet detaching from such a surface.[24,32]

Maximum *vs.* detachment force

As discussed previously, for surface force method (but not for body force), the droplet experiences a maximum force $F_{max} > F_d$. There is much less data available for F_{max} in the literature. Nevertheless, the experimental results from Samuel *et al.* (2011)[16] and Zhu *et al.* (2022)[17] are consistent with our numerical results (Fig. 6).

Our numerical simulations indicate that F_{max} is linearly proportional to ε, *i.e.*,

$$\frac{F_{max}}{\gamma V^{1/3}} = 1.971\varepsilon \quad (6)$$

(dashed blue line, Fig. 6). Our numerical results therefore suggest that F_{max} (unlike F_d) can be related to $\gamma(1 + \cos\theta_r)$ even for hydrophilic surfaces, though more experimental data is required to confirm this.

Detachment *vs.* friction force

It is important to recognize that the lateral F_{fric} acting on a droplet can be very different in magnitude from the vertical F_d discussed in this paper. Furmidge proposed that the lateral friction force acting on the droplet is given by the relation

$$F_{fric} = \pi r\gamma(\cos\theta_r - \cos\theta_a) \quad (7)$$

where θ_a is the advancing contact angle. For superhydrophobic surfaces which have $\theta_a \approx 180°$, $F_{fric} \approx \pi r\gamma(1 + \cos\theta_r)$.[33] Hence, $F_d/F_{fric} = R/r \sim 10$, *i.e.*, it is easier to move a droplet on a superhydrophobic surface by applying a lateral force as compared to a vertical force.

More recently developed surfaces, such as lubricated[21,22] and slippery covalently-attached liquid (SCAL) surfaces,[34] typically exhibit $\theta_r \sim 90°$, $r \sim R$, and $1 + \cos\theta_r \sim 1$, $\cos\theta_r - \cos\theta_a \sim 10^{-3}$.[35–37] Hence, $F_d/F_{fric} \sim 10^3$.

3 Conclusions

Using a combination of numerical simulations and simple geometrical arguments, we were able to explain the observed detachment forces reported by various research groups spanning over a wide range of experimental parameters from micron- to millimetric-sized droplets and force magnitudes ranging from nano- to millinewtons. We also showed that for highly hydrophobic surfaces with $\theta_r > 140°$, the normalized detachment force $F_d/\pi R$ is equivalent to the Young–Dupre adhesion $\gamma(1 + \cos\theta_r)$.

Author contributions

X. Q. K. performed the experiments here. D. D. conceptualized the project, performed numerical and theoretical analysis, supervised the research, and wrote the manuscript.

Conflicts of interest

There are no conflicts to declare.

Acknowledgements

We thank Sadullah and co-workers for sharing their data with us and for their valuable comments.

Notes and references

1 P.-G. Gennes, F. Brochard-Wyart and D. Quéré, *Capillarity and wetting phenomena: drops, bubbles, pearls, waves*, Springer, 2004.
2 D. Beysens, *The physics of dew, breath figures and dropwise condensation*, Springer, 2022, vol. 994.
3 B. Derby, *Annu. Rev. Mater. Res.*, 2010, **40**, 395–414.
4 C. Furmidge, *J. Colloid Sci.*, 1962, **17**, 309–324.
5 C. Cao, Y.-Y. Song, Z.-L. Zhou, L.-D. Cao, F.-M. Li and Q.-L. Huang, *Soft Matter*, 2018, **14**, 8030–8035.
6 H.-J. Butt, I. V. Roisman, M. Brinkmann, P. Papadopoulos, D. Vollmer and C. Semprebon, *Curr. Opin. Colloid Interface Sci.*, 2014, **19**, 343–354.
7 D. Daniel, M. Vuckovac, M. Backholm, M. Latikka, R. Karyappa, X. Q. Koh, J. V. I. Timonen, N. Tomczak and R. H. A. Ras, *Commun. Phys.*, 2023, **6**, 152.
8 Y. Jiang and C.-H. Choi, *Adv. Mater. Interfaces*, 2021, **8**, 2001205.
9 M. E. Schrader, *Langmuir*, 1995, **11**, 3585–3589.
10 R. Tadmor, R. Das, S. Gulec, J. Liu, H. E. N'guessan, M. Shah, P. S. Wasnik and S. B. Yadav, *Langmuir*, 2017, **33**, 3594–3600.
11 C. W. Extrand, *Langmuir*, 2017, **33**, 9241–9242.

12 S. Gulec, S. Yadav, R. Das and R. Tadmor, *Langmuir*, 2017, **33**, 13899–13901.
13 M. S. Sadullah, Y. Xu, S. Arunachalam and H. Mishra, *arXiv*, 2023, preprint, arXiv:2307.12527, DOI: **10.48550/arXiv.2307.12527**.
14 D. Daniel, C. L. Lay, A. Sng, C. J. J. Lee, D. C. J. Neo, X. Y. Ling and N. Tomczak, *Proc. Natl. Acad. Sci. U. S. A.*, 2019, **116**, 25008–25012.
15 V. Liimatainen, M. Vuckovac, V. Jokinen, V. Sariola, M. J. Hokkanen, Q. Zhou and R. H. A. Ras, *Nat. Commun.*, 2017, **8**, 1798.
16 B. Samuel, H. Zhao and K.-Y. Law, *J. Phys. Chem. C*, 2011, **115**, 14852–14861.
17 Z. Zhu, Y. Jiang and J. W. Drelich, *Langmuir*, 2022, **38**, 8456–8461.
18 M. Jamali, A. Moghadam, H. V. Tafreshi and B. Pourdeyhimi, *Appl. Surface Sci.*, 2018, **456**, 626–636.
19 J. F. Padday and A. R. Pitt, *Philos. Trans. R. Soc., A*, 1973, **275**, 489–528.
20 D. Quéré, *Phys. A: Stat.*, 2002, **313**, 32–46.
21 T.-S. Wong, S. H. Kang, S. K. Y. Tang, E. J. Smythe, B. D. Hatton, A. Grinthal and J. Aizenberg, *Nature*, 2011, **477**, 443–447.
22 A. Lafuma and D. Quéré, *Europhys. Lett.*, 2011, **96**, 56001.
23 C. Thenarianto, X. Q. Koh, M. Lin, V. Jokinen and D. Daniel, *Langmuir*, 2023, **39**, 3162–3167.
24 D. Daniel, S. S. Goh, T. N. B. Truong, X. Q. Koh and N. Tomczak, *Adv. Mater. Interfaces*, 2021, **8**, 2001203.
25 D. Daniel, *Codes for Solving Young–Laplace Equation*, 2019, accessed: 2018-08-16, **https://github.com/ddaniel331/laplace_solver**.
26 D. Daniel, *Codes for Solving Young–Laplace Equation (Body force)*, 2023, accessed: 2023-08-18, **https://github.com/ddaniel331/laplace_pendant**.
27 D. Daniel, *Replication Data for: Droplet detachment force and its relation to Young–Dupre adhesion*, 2023, accessed: 2023-08-16, **https://doi.org/10.7910/DVN/3M6VQX**.
28 A. J. Meuler, J. D. Smith, K. K. Varanasi, J. M. Mabry, G. H. McKinley and R. E. Cohen, *ACS Appl. Mater. Interfaces*, 2010, **2**, 3100–3110.
29 J. D. Smith, R. Dhiman, S. Anand, E. Reza-Garduno, R. E. Cohen, G. H. McKinley and K. K. Varanasi, *Soft Matter*, 2013, **9**, 1772–1780.
30 M. J. Kreder, D. Daniel, A. Tetreault, Z. Cao, B. Lemaire, J. V. I. Timonen and J. Aizenberg, *Phys. Rev. X*, 2018, **8**, 031053.
31 G. H. McKinley, HML Report No. 05-P-04, 2005.
32 D. Daniel, A. Y. T. Chia, L. C. H. Moh, R. Liu, X. Q. Koh, X. Zhang and N. Tomczak, *Commun. Phys.*, 2019, **2**, 105.
33 F. Schellenberger, N. Encinas, D. Vollmer and H.-J. Butt, *Phys. Rev. Lett.*, 2016, **116**, 096101.
34 I. J. Gresham and C. Neto, *Adv. Colloid Interface Sci.*, 2023, 102906.
35 D. Daniel, J. V. I. Timonen, R. Li, S. J. Velling and J. Aizenberg, *Nat. Phys.*, 2017, **13**, 1020–1025.
36 D. Daniel, J. V. I. Timonen, R. Li, S. J. Velling, M. J. Kreder, A. Tetreault and J. Aizenberg, *Phys. Rev. Lett.*, 2018, **120**, 244503.
37 A. Keiser, P. Baumli, D. Vollmer and D. Quéré, *Phys. Rev. Fluids*, 2020, **5**, 014005.